Fabrication and Testing of a Shape Memory Alloy Actuated Reconfigurable Wing

Justin K. Strelec[a], Dimitris C. Lagoudas[a]
[a]Aerospace Engineering Department, Texas A&M University, College Station, TX 77843-3141

ABSTRACT

The unique thermal and mechanical properties exhibited by shape memory alloys (SMAs) present exciting design possibilities in the field of aerospace engineering. When properly trained, SMA wires act as linear actuators by contracting when heated and returning to their original shape when cooled. These SMA wire actuators can be attached to points on the inside of an airfoil, and can be activated to alter the shape of the airfoil. This shape-change can effectively increase the efficiency of a wing in flight at several different flow regimes. Design optimization has previously been conducted to determine the placement of actuators within the reconfigurable airfoil. A wind tunnel model reconfigurable wing was fabricated based on the design optimization to verify the predicted structural and aerodynamic response. Wind tunnel tests indicated an increase in lift for a given flow velocity and angle of attack by activating the SMA wire actuators. The pressure data taken during the wind tunnel tests followed the trends expected from the numerical pressure results.

1. INTRODUCTION

Aircraft design involving fixed wing structures often involves a sacrifice in design point efficiency to account for off-design flight conditions. These compromises can be eliminated with the implementation of a wing that can adapt to its current flow condition.

One factor that greatly influences a wing's efficiency at a particular flow regime is the shape of its cross-section, or airfoil. Some airfoils are aerodynamically efficient at subsonic speeds, but typically create undesirable shock waves early in the transonic regime. Other airfoils are tailored to minimize wave drag near the speed of sound, but do not produce favorable pressure distributions at low subsonic speeds. Typical plots of favorable pressure distributions in subsonic and transonic regimes are shown in Figure 1 [1].

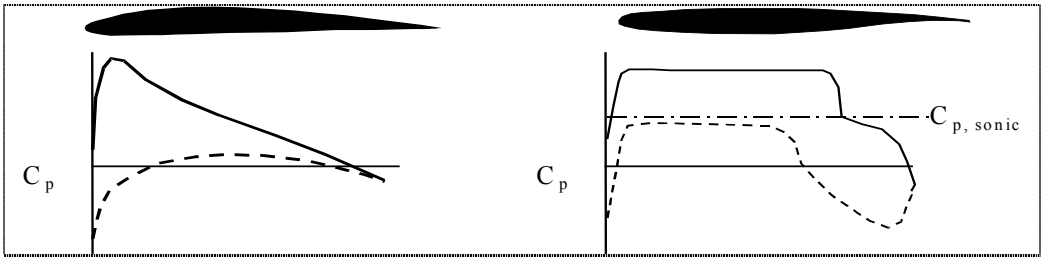

Figure 1. Pressure plots of typical subsonic (left) and transonic (right) airfoils in their respective flow regimes

Airfoils are typically designed with a primary flight condition in mind, for example cruise. These airfoils are generally sub-optimal for the design point because they are fixed and must be used at takeoff, landing, climb, and descent in addition to the design point condition. It would be

desirable to have an airfoil with the ability to adapt to its current flow regime and alter its shape to remain efficient at any speed [2-5].

The primary focus of this research is to control the physical shape of an airfoil in a global sense. That is, to create a reconfigurable wing whose airfoil can achieve the potential large-scale deflections necessary to maintain high efficiency as flow conditions change. A high force, high displacement actuator is needed to achieve the deformations required for full airfoil reconfigurability. Current research of shape memory alloys has revealed that they can be used very effectively as lightweight, high force, large deflection, quick response actuators, and may be ideally suited for the reconfigurable airfoil application [6-10].

Shape memory alloys (SMA) are set apart from other metals by their unique crystalline characteristics [11]. They exhibit one of two crystalline lattice structures depending on the applied stress and temperature. The low temperature phase, martensite, is a simple monoclinic arrangement and the high temperature phase, austenite, is a body centered cubic arrangement. The material properties of SMA are dependant on the amount of each phase present at a given time [12].

The martensitic phase of an SMA can have a lattice arrangement in one of 24 variants depending on the local stress field, and can appear as twinned or detwinned. In its martensitic phase, SMA can be deformed easily as these variants interchange to those that align more favorably with the local stress field. Heating the SMA will force a return to its austenitic phase and bring the SMA back to its original macroscopic shape. The recovered strain is called the transformation strain. Two-way shape memory effect can be achieved by inducing a plastic deformation in the material such that a transformation into martensite results in a macroscopic shape change without an applied stress. This is called two-way shape memory effect because macroscopic shape change occurs in both the heating and cooling directions, even in the absence of external stresses [13].

Because they are both commonly attainable and easy to implement as linear actuators, SMA wires are used in this research. Two-way trained SMA wire actuators are attached to points on the inside of an airfoil after they have been cooled below the martensitic finish temperature. When the wires are heated above the austenitic start temperature, they begin to contract, recovering the transformation strain and deforming the airfoil. Upon cooling below the martensitic finish temperature, the SMA actuators are brought back to their original configuration, returning the airfoil to its original shape.

The design and analysis of the SMA-actuated reconfigurable airfoil and the optimal placement of SMA actuators within the wing have been presented previously [14]. The thermomechanical response of the wing was modeled using a finite element analysis coupled with a computational fluid dynamics code to accurately predict the mechanical deformation of the wing under actuator and aerodynamic loads. The thermomechanical response of the SMA actuators was modeled using the user-defined subroutine UMAT [15].

This paper will examine the fabrication and testing of an SMA-actuated reconfigurable wing with the intent of maximizing the wing's lift-to-drag ratio (c_l/c_d) at a subsonic flight condition. A demonstration of airfoil reconfigurability will show the ability of SMA actuators to modify the global shape of an existing airfoil. Actuator development, skin material selection, structural analyses, no-flow static bench tests, and wind tunnel experiments will be discussed.

2. RECONFIGURABLE WING FABRICATION AND TESTING

The objective of the prototype reconfigurable wing experiment is to first demonstrate the reconfigurable properties of the wing and second to verify the structural and aerodynamic models.

Design optimization was used to place the wires in the prototype wing, but simplifications were made in the process to account for design restrictions within the wing.

2.1. SMA Wire Actuator Training and Preparation

To achieve the desired actuator effect with shape memory alloy wires, they must exhibit two-way training. There are several ways to achieve two-way SME in shape memory alloy wires, as described by deBlonk et al [16]. In the current work, two-way training is achieved by first deforming the specimen under appropriate load in the martensitic phase. Then, the specimen is heated to its austenitic phase and cooled back to a martensitic phase. After many cycles, the specimen will begin to exhibit two-way shape memory effect. The K type NiTiCu SMA wires used in this work were 152 mm in length and had a diameter of 0.59 mm. The wires were trained by loading them to 372 MPa and cycling fifty 0ºC to 100ºC thermal cycles.

In this work, the wires are heated by electrical current and cooled by natural convection. The wires were put through a series of tests and demonstrated recoverable transformation strain of about 3.7%. A differential scanning calorimeter (DSC) was used to determine the start and finish austenite and martensite transformation temperatures. Quasi-static tests were conducted on a load frame to determine the modulus of elasticity for both the martensitic and austenitic phases of the material. A summary of the resulting material properties is shown in Table 1.

Table 1. SMA wire material properties

A^{0s}	53.7 °C
A^{0f}	59.5 °C
M^{0s}	45.7 °C
M^{0f}	39.3 °C
E_A	65 GPa
E_M	20 GPa

2.2. Reconfigurable Wing Model Construction

Two generations of models were constructed. The first generation used a stainless steel skin over aluminum ribs. The stainless steel wing showed promising results structurally, but problems in manufacturing led to undesirable aerodynamic characteristics. In addition, the steel skin had to be extremely thin to allow for deflection by the SMA, which caused the skin to buckle in some situations. Following this wing, and using the lessons learned, a new model was constructed. Several design enhancements were made after the construction of the first generation reconfigurable wing. An actuator access panel was included so that proper tensioning of the SMA wires could take place after assembly, and visual observation of the SMA actuation could be conducted during bench tests.

A Stratasys FDM 3000 rapid prototyping machine was used to build the second-generation model's skin. The major benefit of this manufacturing method is that ABS, a common engineering plastic, is used to create the model. ABS is a durable, high-strength modeling material that can be machined, sanded, drilled, painted, and glued after the model is built. For the reconfigurable wing

model, this allows the drilling of pressure ports, the adhesion of pressure tubes to the skin, and the sanding of the skin to achieve a smooth aerodynamic surface.

Another benefit of using a fused deposition modeling (FDM) generated plastic skin is that the thickness can be varied throughout the model, whereas the steel skin had a constant thickness. By changing the thickness of the skin, precise areas on the wing can be tailored to be more or less stiff than the rest of the wing. This variable skin thickness could be used in future efforts as a design optimization tool.

The rapid prototyping method of construction allowed some design simplifications, as shown in Figure 2. Where silver solder was needed to create attachment points on the inner surface of the steel skin, a raised plastic strip with holes in it was easily created by the FDM process. Also, the skin thickness was increased at the rib attachment points to create a flat surface so that the rib would have a flush contact surface against the skin. This decreased the complexity of rib manufacturing by eliminating the need for a shaped rib surface.

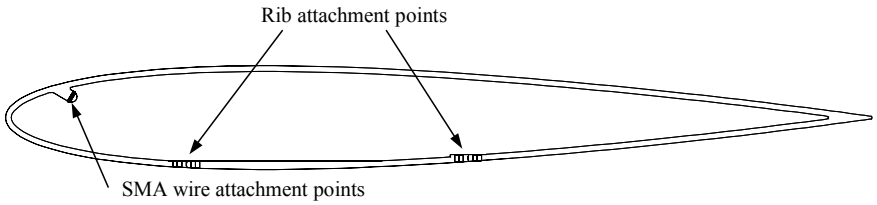

Figure 2. Second generation wing model drawing

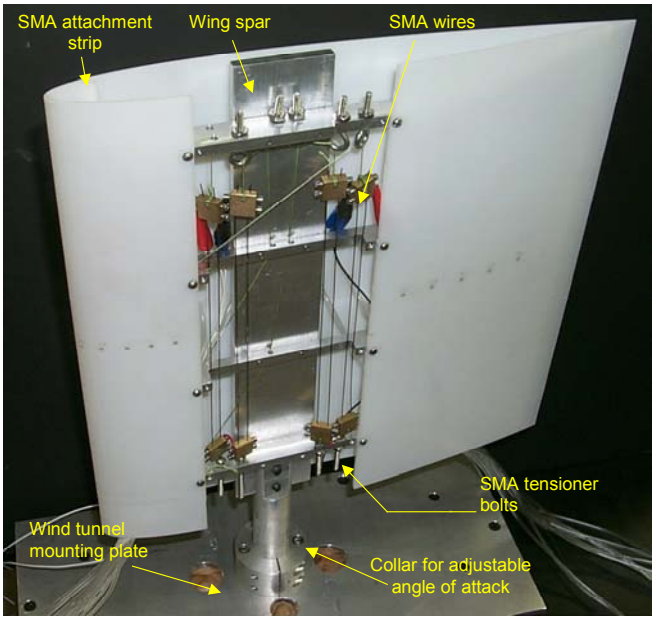

Figure 3. Second Generation Prototype Wind Tunnel Model

The second-generation reconfigurable wing model is shown in Figure 3. Higher wing skin stiffness was desired for the second-generation model, and eight SMA wires were employed to provide enough force to deflect this wing. Figure 3 also shows the layout of the internal structural members of the wing.

2.2.1. Structural Analysis and Static Experiments

The thickness of the skin in the new wing design had to be adjusted from the original design because the ABS plastic is not as stiff as the original stainless steel material. The ABS had a Young's modulus of approximately 4.2 GPa as opposed to stainless steel's 200 GPa. A finite element model had already been developed for use in analyzing the steel skinned prototype. This FEM model was implemented in ABAQUS with the user-defined subroutine UMAT [15]. The model was modified to use ABS as the skin material and the thickness was increased from 0.254 mm for the steel skin to approximately 2.54 mm for the ABS skin. The final thickness was chosen using the FEM analysis with an ABS skin. Several cases were analyzed, and 2.54 mm thick ABS most nearly reproduced the response of the steel skin. The increase in skin thickness also created an environment where buckling would be less likely to occur. The FEM analysis is shown in Figure 4. A trailing edge deflection of 5.0 mm was predicted when the SMAs were fully actuated.

Figure 4. Undeformed (black) vs. Deformed (red) Configurations Obtained from FEM

Figure 5 shows a cross-sectional view of the aft wing section in an undeformed state. Figure 6 shows an identical camera angle of the model in a fully actuated position, and shows a trailing edge deflection of approximately 6 mm. The difference between the predicted deflection and the actual deflection arises from the rough experimental measurement technique and the complex factors in design as well as the fact that the numerical solution assumed a uniform and homogeneous skin material, when in actuality this assumption is not strictly correct.

Figure 5. Trailing edge, undeformed state

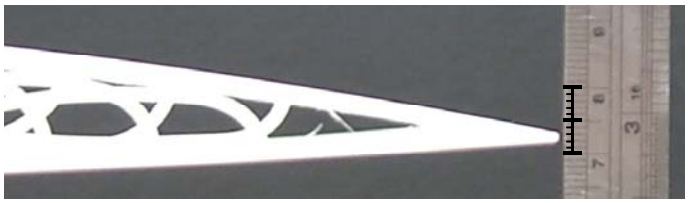

Figure 6. Trailing edge, actuated state

2.3 Reconfigurable Wing Wind Tunnel Experiments

Wind tunnel tests were performed in the Texas A&M University low speed 2'x3' wind tunnel. Figures 7 and 8 show the wing mounted in the tunnel.

Figure 7. Reconfigurable wing mounted in wind tunnel

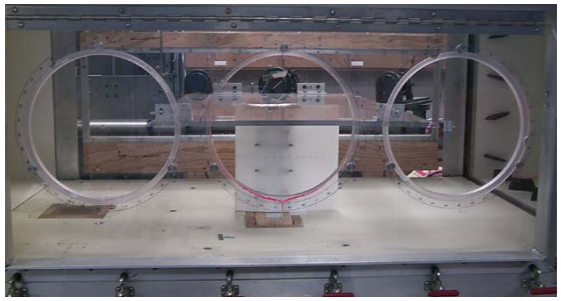

Figure 8. Side view of reconfigurable wing mounted in wind tunnel

The goal of these tests was to measure the pressure distribution over the original and deformed airfoil shapes to verify that an increase in lift was being achieved. The pressure data must be reduced into a non-dimensional coefficient of pressure term, C_P. C_P is calculated as follows

$$C_P = \frac{p - p_\infty}{\frac{1}{2}\rho V^2} = \frac{p - p_\infty}{q} \tag{1}$$

where $p - p_\infty$ is the differential pressure measured through pressure ports as discussed below. This differential pressure is normalized with respect to the dynamic pressure, q, which is a function of density, ρ, and free-stream velocity, V. If the flow is incompressible and no Mach effects are observed, the C_P pressure distribution should be the same regardless of flow velocity.

The non-dimensional normal force coefficient (normalized with respect to the chord length, c) can be determined from the pressure distribution data by integrating between the upper and lower pressure distribution curves as follows:

$$c_n = \int_0^1 \left(C_{p,lower} - C_{p,upper}\right) d\left(\frac{x}{c}\right) \tag{2}$$

Finally, to calculate the coefficient of lift for a given angle of attack, the following calculation is performed:

$$c_l = c_n \cos\alpha \tag{3}$$

An electronic scanning pressure (ESP) module was used to capture pressure data from 29 ports along the upper and lower surfaces of the wing. More ports were desirable to increase resolution, but available space within the model limited the number. Figure 9 shows the actual configuration of the lower surface pressure ports.

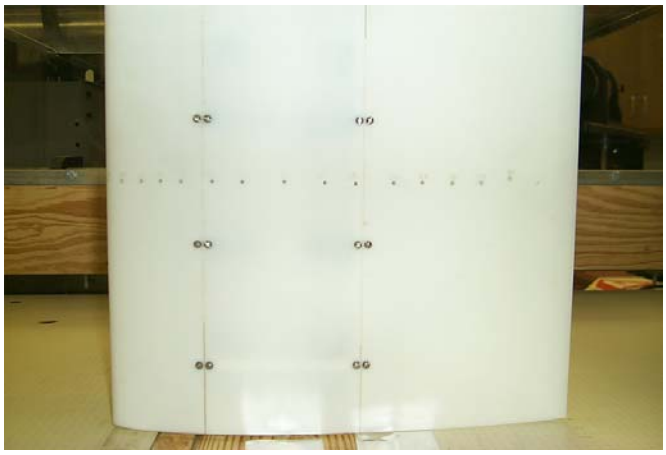

Figure 9. Lower surface of wing showing pressure port locations

The wind tunnel tests were conducted at flow velocities of 8.5, 10.2, and 12.0 m/s. The ambient test conditions were a temperature of 18° C, an atmospheric pressure of 101.1 kPa, and an air density of 1.21 kg/m^3. The model was swept through 0, 5, and 10 degrees angle of attack (AOA). An additional 16.0 m/s velocity run was preformed at 0 degrees angle of attack to further examine performance at higher velocities. For each test case, data was taken in the undeformed configuration. Then, the wing was actuated and data was taken in the deformed configuration.

2.4. Wind Tunnel Experimental Results

The following series of figures shows the effect of changing the angle of attack of the wing. Figures 10 and 11 show the undeformed and deformed cases, respectively, at 8.5 m/s flow velocity. Similar results are available for other velocities, but only 8.5 m/s is shown here for conciseness. The figures show that the area bounded by the upper and lower C_P lines increases with an increase in angle of attack, as expected.

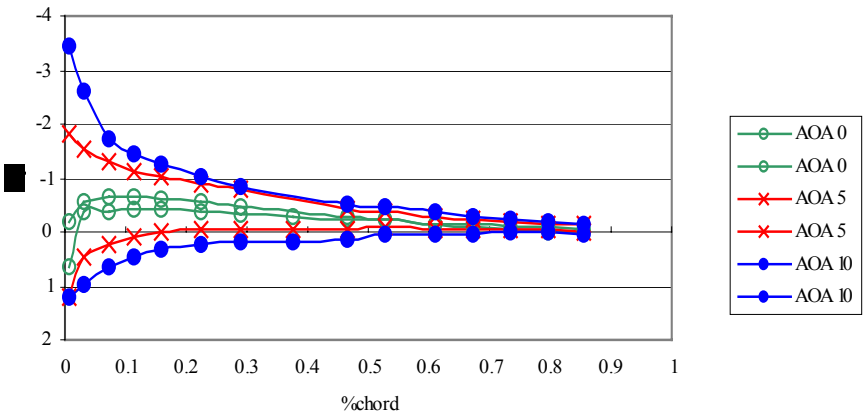

Figure 10. Angle of attack sweep, undeformed case, 8.5 m/s

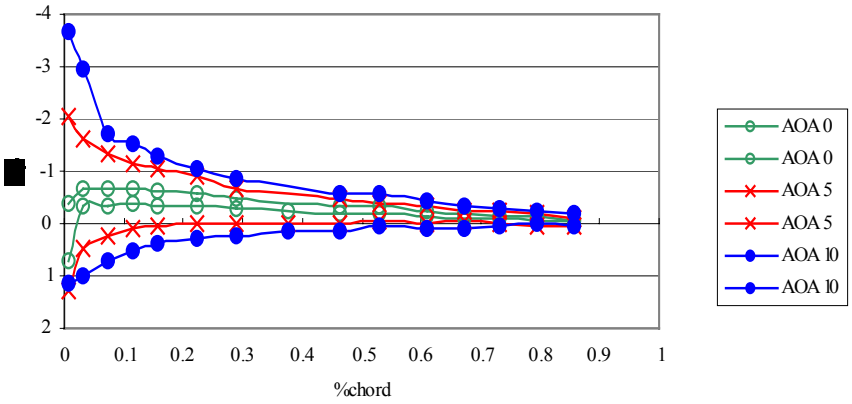

Figure 11. Angle of Attack sweep, deformed case, 8.5 m/s

The next series of figures shows the deformed vs. undeformed case pressure distributions for each angle of attack. Figures 12, 13, and 14 show this comparison at 0, 5, and 10 degrees angle of attack, respectively. At zero degrees angle of attack, the improvement in pressure distribution is clear. However, as the angle of attack increases, this improvement seems to decrease. Curves were fit to the data and the area between the upper and lower surfaces was computed to find the normal force coefficient, c_n. This was then used to calculate c_l as shown in equation 7. Table 2 shows the results of those calculations.

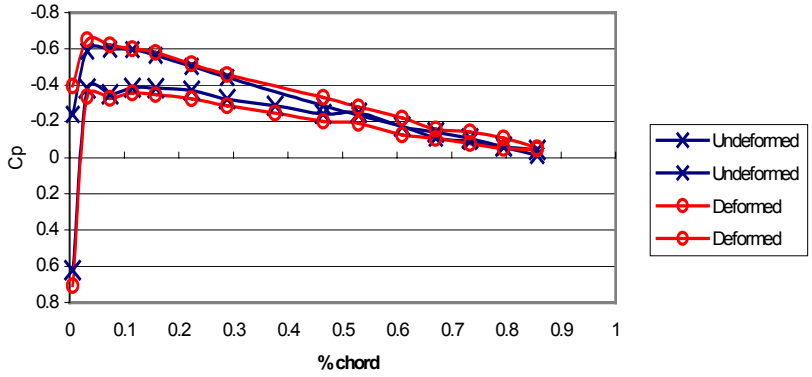

Figure 12. Effects of deformation on pressure distribution, AOA 0

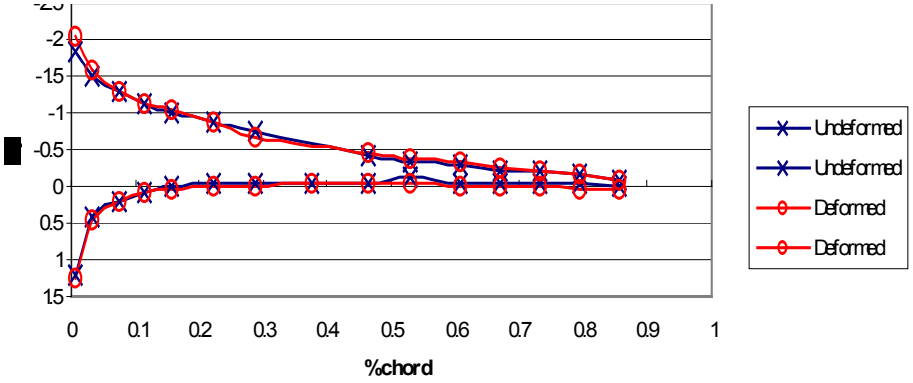

Figure 13. Effects of deformation on pressure distribution, AOA 5

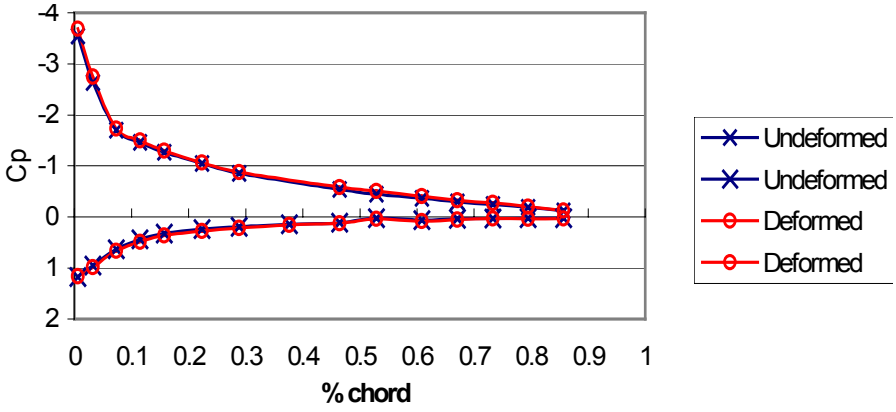

Figure 14. Effects of deformation on pressure distribution, AOA 10

Table 2. Change in lift coefficient due to SMA actuation

Angle of Attack	Lift Coefficient-Undeformed case	Lift Coefficient-Deformed Case	Δc_l	% increase
0	0.072	0.134	0.062	N/A
5	0.510	0.555	0.045	8.79%
10	0.837	0.892	0.055	6.59%

From the quantitative analysis, it is clear that the greatest improvement in c_l is at zero degrees angle of attack, with an increase of about 0.062. At five and ten degrees angle of attack, increases of 0.045 and 0.055, respectively, were calculated. A comparison of the Δc_l for the computational and experimental data is shown in Figure 25. The experimental data shows a Δc_l that is approximately half that predicted by the numerical data.

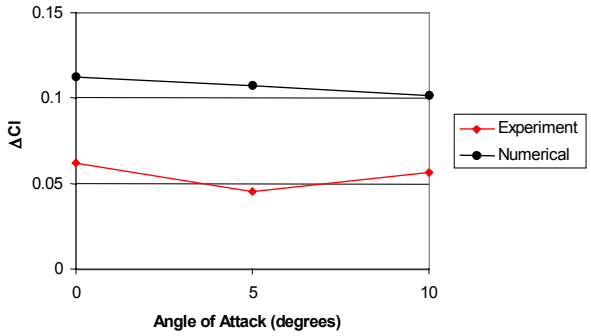

Figure 15. Δc_l vs. angle of attack for experimental and numerical data

2.5. Comparison of Experimental and Numerical Results

Although it is not the focus of this paper, it is important to note the computational fluid dynamics (CFD) tools uses to produce numerical analysis of these airfoils. A panel method solver, XFOIL, was used iteratively with the FEM solver until the solution converged. The purpose of this method was to correctly solve the fluid structure interaction that occurs in situations where the solid can and is deformed by the flow around it. CFD calculations were performed on the original and deformed airfoil shapes for 0, 5, and 10 degrees angle of attack. The next six figures show an overlay of these numerical pressure distributions over the average pressure distributions calculated from the velocity sweep data. Figures 16 and 17 show the comparison of experimental vs. numerical pressure data at zero degrees angle of attack for the undeformed and deformed cases. Figures 18 and 19 show similar data for five degrees angle of attack, and Figures 20 and 21 show the pressure comparison data for ten degrees angle of attack. Note that the solid line represents numerical results and dots represent experimental results.

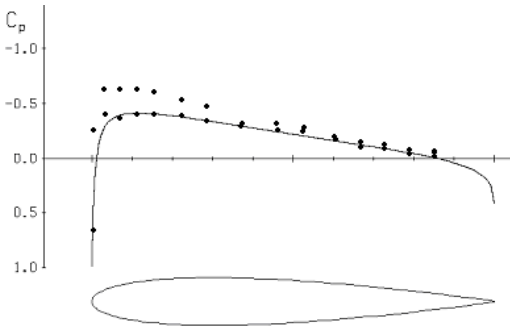

Figure 16. Numerical vs. experimental pressures, undeformed case, 0° angle of attack

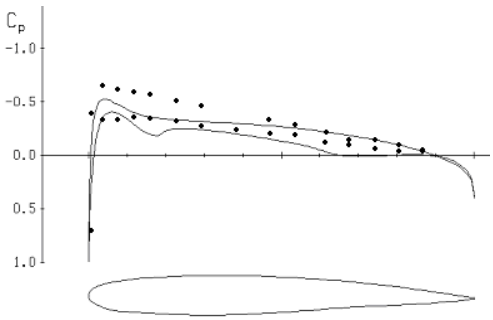

Figure 17. Numerical vs. experimental pressures, deformed case, 0° angle of attack

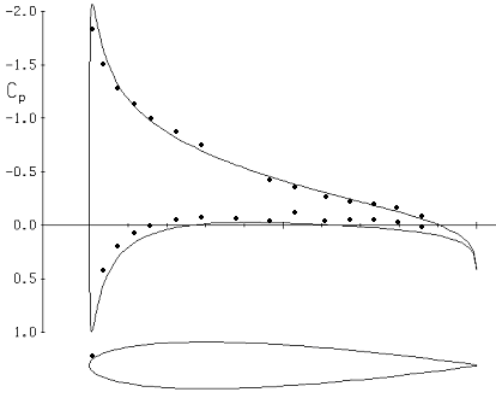

Figure 18. Numerical vs. experimental pressures, undeformed case, 5° angle of attack

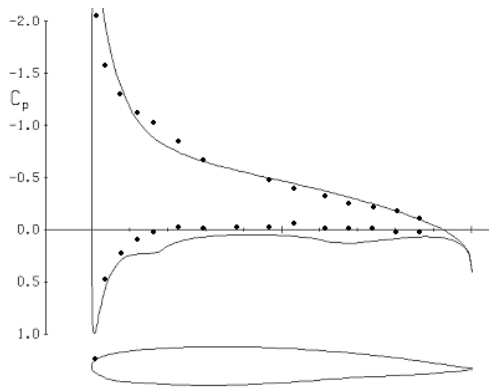

Figure 19. Numerical vs. experimental pressures, deformed case, 5° angle of attack

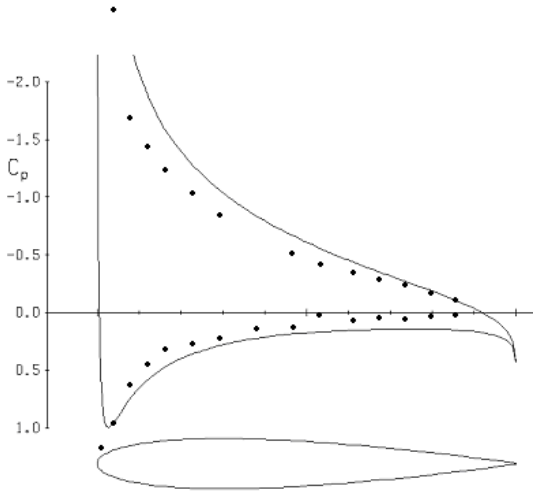

Figure 20. Numerical vs. experimental pressures, undeformed case, 10° angle of attack

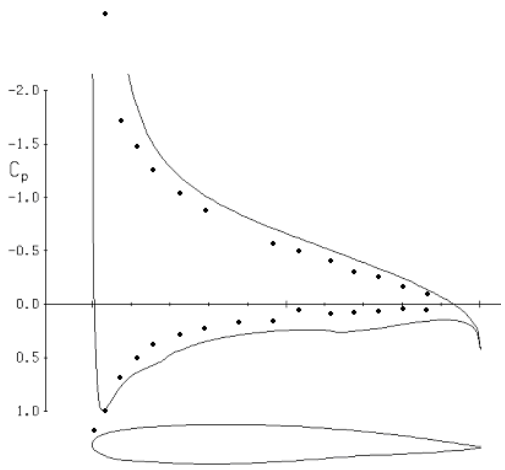

Figure 21. Numerical vs. experimental pressures, deformed case, 10° angle of attack

The experimental pressure distribution matches the numerical pressure distribution well for the undeformed case. For the deformed case, however, it is necessary to note that while the experimental pressure distribution follows the general trend of the predicted numerical distribution, some details of the numerical analysis do not appear in the experimental results. This is due to the numerical solution encompassing all aspects of the skin such as perfectly fixed boundary conditions at the rib attachment points. In the experimental model the fine details of the skin were lost in manufacturing. There are several causes for the discrepancy between numerical and experimental results. Two major reasons are the lack of resolution in pressure taps and the open wing tips. Fully 10% of the wing at the trailing edge was not instrumented due to structural interference. The leading edge also may not have been instrumented finely enough to capture the true behavior of the leading edge pressure distribution. These combined could have resulted in a significant decrease in both c_l and Δc_l for the experimental cases.

The wing tips were left open and placed nearly flush against either wall of the wind tunnel in order to prevent air from entering the wing. However, as the angle of attack increased, the wing tips separated slightly from the wind tunnel walls, allowing some air to enter the wing. This served to cool the SMA wires, especially in the higher velocity cases, and cause the wire temperature to not fully reach the austenite finish temperature. This indicated that in the high angle of attack cases, the expected wing deformations might not have been achieved. Despite this, an increase in c_l was still observed at all angles of attack, indicating the successful operation of the SMA reconfigurable wing in wind tunnel conditions.

3. CONCLUSIONS

A reconfigurable wing model was developed to verify the structural and aerodynamic response predicted by the computational analyses. The FDM prototype reconfigurable wing model was developed to overcome the unforeseen manufacturing difficulties and design flaws of the first generation model. A rapid prototyping machine was used to create an ABS plastic skin with the accurate initial airfoil shape. The thickness of the skin was increased to compensate for the lower elastic modulus of the new material. This extra thickness also served to prevent the buckling that was seen in the first generation model. Actuator attachment points were designed into the skin, eliminating the need for soldered attachment points.

Structural and aerodynamic analyses were performed on the second-generation reconfigurable wing model. The structural analysis predicted a trailing edge deflection of approximately 5.0 mm. For comparison purposes, the experimental trailing edge deflection measured in the bench test was about 6.0 mm.

Wind tunnel tests were conducted to obtain experimental pressure distribution data over the original wing shape and the deformed wing shape. These experimental pressure distributions compared well to the numerical pressure distributions for the undeformed case. For the deformed case, the experimental data matched less closely, but still followed the expected trends. The lift coefficient increased by 0.062 at zero degrees angle of attack when the wing was deformed, by 0.045 at five degrees angle of attack, and by 0.055 at ten degrees angle of attack. This is comparable to the lift increases seen by other researchers. Scherer, et al [17], for instance, achieved a Δc_l that ranged from 0.03 to 0.09, based on SMA-actuated trailing edge deflections. However, the achieved Δc_l is considerably less than the Δc_l predicted by the numerical models.

4. ACKNOWLEDGEMENTS

The authors acknowledge the financial support of the U.S. Air Force Office of Scientific Research (grant no. F4 9620-01-1-0196). The authors would like to acknowledge Dr. Othon Rediniotis and Dr. John Valasek for their assistance in this project, and Luke Penrod for his assistance with final editing.

5. REFERENCES

[1] Anderson J D 1978 *Introduction to Flight* (New York: McGraw-Hill)

[2] Austin F, Rossi M J, Van Nostrand W, Knowles G and Jameson A 1994 Static Shape Control for Adaptive Wings *AIAA Journal* **32** 1895-1901

[3] Pern N J and Jacob J D 1999 Aerodynamic Flow Control Using Shape Adaptive Surfaces *Proc. 1999 ASME Design Engineering Technical Conferences (Las Vegas, NV)*

[4] Munday D and Jacob J 2001 Active Control of Separation on a Wing with Conformal Camber *39th AIAA Aerospace Sciences Meeting and Exhibit, AIAA 2001-0293 (Reno, NV)*

[5] Bein T, Hanselka H and Breitbach E 2000 An Adaptive Spoiler to Control the Transonic Shock *Smart Materials and Structures* **9** 141-148

[6] Kudva J, Jardin P, Martin C and Appa K 1996 Overview of the ARPA/WL 'Smart Structures and Materials Development – Smart Wing' Contract *3rd SPIE Symposium on Smart Structures and Materials (San Diego CA)*

[7] Gilbert W W 1981 Mission Adaptive Wing System for Tactical Aircraft *Journal of Aircraft* **18** 597-602

[8] Garner L J, Wilson L N, Lagoudas D C and Rediniotis O K 2000 Development of a Shape Memory Alloy Actuated Biomimetic Vehicle *Smart Materials and Structures* **9** 673-683

[9] Kudva J N, Martin C A, Scherer L B, Jardine A P, McGowan A R, Lake R C, Sendeckyj G and Sanders B 1999 Overview of the DARPA/AFRL/NASA Smart Wing Program *SPIE Conference on Industrial and Commercial Applications of Smart Structures Technologies* **3674**

[10] Martin C A, Bartley-Cho J, Flanagan J and Carpenter B F 1999 Design and Fabrication of Smart Wing Wind Tunnel Model and SMA Control Surfaces *SPIE Conference on Industrial and Commercial Applications of Smart Structures Technologies* **3674**

[11] Beauchamp C, Nadolink R and Dean L 1992 Shape Memory Alloy Articulated (SMAART) Control Surfaces *ADPA/AIAA/ASME/SPIE Conference on Active Materials and Adaptive Structures (Alexandria, VA)*

[12] Saburi T 1999 Ti-Ni Shape Memory Alloys, in *Shape Memory Alloys* (Cambridge, UK: Cambridge University Press) eds Otsuka K and Wyman C M pp. 49-96

[13] Jackson C M, Wagner H J and Wasilewski R J 1972 55-Nitinol – The Alloy with A Memory: Its Physical Metallurgy, Properties, and Applications *NASA (Washington D.C.)*

[14] Lagoudas D C, Strelec J K, Yen J and Khan M A 2000 Intelligent Design Optimization of a Shape Memory Alloy Actuated Reconfigurable Wing *Proceedings of the SPIE 2000 Conference on Smart Structures and Materials* **3984** 338-348

[15] Lagoudas D C, Bo Z and Qidwai M A 1996 A unified thermodynamic constitutive model for SMA and finite element analysis of active metal matrix composites *Composite Materials and Structures* **3** 153-179

[16] De Blonk B J and Lagoudas D C 1998 Actuation of Elastomeric Rods with Embedded Shape Memory Alloy Wire Actuators *Smart Materials and Structures* **7** 771-783
[17] Scherer L B, Martin C A, West M, Florance J P, Wieseman C D, Burner A W and Fleming G A 1999 DARPA/AFRL/NASA Smart Wing Second Wind Tunnel Test Results *SPIE Conference on Industrial and Commercial Applications of Smart Structures Technologies* **3674**